Pure Appl. Geophys. 180 (2023), 59–68

https://doi.org/10.1007/s00024-022-03216-4

Pure and Applied Geophysics

Uncertainties in Finite-Fault Slip Inversions, Part II: Fault Discretization and Parameterization of Slip Function

Igor A. Beresnev[1]

Abstract—To maintain a stable and computationally feasible inverse problem, standard methods of inversion of ground motions for slip distribution on earthquake faults have to limit the size of the fault-discretization grid, with no clearly established criteria for setting the cell size. The subfault dimensions typically scale with earthquake magnitude. Also, the solution of a linear matrix equation, being the basis for the standard inversion techniques, assumes the slip weight on subfaults to be the only rupture parameter to solve for. This approach does not consider the fact that fault radiation is controlled by two independent rupture parameters – the slip U and peak slip rate v_m – except at very low frequencies. These two parameters trade off with each other. Sensitivities of slip images to the selection of the grid and the assumption of a particular slip velocity (through a subfault's rise time) cause ambiguities in the inverted models. Such sensitivities can be investigated by discretizing the representation integral of elasticity. For a heterogeneous fault, containing both a deterministic and a stochastic components, the subfault size of approximately 3×2.5 km leads to significant unphysical oscillations in the radiated ground-velocity pulse, caused by imprecise representation of the continuous integral; any coarser grid will cause distortions of the true slip distribution. The trade-off between U and v_m results in offsetting large changes in subfault slip by relatively minor changes in slip velocity. The consequences of inadequate choices of mesh size and fixing the value of slip velocity (via slip duration), inevitable in the formulation of the matrix inversion, are the distortions of true slip of unknown severity. The artifacts produced are exacerbated by the use of the triangular slip-velocity function, compared to the omega-square one, as well as by the retention of only the far-field terms in the matrix equation.

Keywords: Fault-slip distribution, source time function, earthquake slip, fault-slip velocity.

1. Introduction

In two earlier publications (Beresnev, 2003, 2013), the author discussed two sources of uncertainty in the standard inversions of seismic data for slip on finite earthquake faults, whose effects on slip images often are not explicitly addressed. The standard method of inversion, followed by the majority of the studies, is based on the solution of a linear matrix equation, in which slip weights on subfaults are the only rupture parameters solved for (Hartzell & Heaton, 1983, their Eq. 2; Hartzell et al., 2007, p. 1911). One source of uncertainty is the assumed discretized-cell size on the plane, and the other is the assumption that the time history of slip is a function of only one parameter – the final (static) offset.

Standard inversions for slip distributions are now routinely published for every major earthquake in the world, while the issues raised earlier still need further investigation. An exact analytical tool that lends itself to such a specific sensitivity analysis is the representation theorem for the seismic source, allowing calculation of source effect of any complexity in its exact form at any distance from the fault.

The basis for the canonical formulation of the linear matrix inversion (Hartzell & Helmberger, 1982, their equation on p. 578; Heaton, 1982, his equation A2) is the elastodynamic representation integral that is succinctly written as

$$u_n(\mathbf{x}, t) = \iint_{\Sigma} m_{pq} * G_{np,q} d\Sigma, \qquad (1)$$

where $u_n(\mathbf{x}, t)$ is the nth component of particle displacement in the radiated field at an observation point $\mathbf{x}$, m_{pq} are the components of the moment-density tensor, G_{np} is the Green's tensor for the geometry of interest, the comma denotes differentiation with respect to the coordinate ξ_q belonging to the fault surface Σ, and the asterisk is the temporal convolution operator (Aki & Richards, 1980, their Eq. 3.19). With $G_{np,q}$ for a homogeneous elastic space, the

[1] Department of Geological and Atmospheric Sciences, Iowa State University, 253 Science I, 2237 Osborn Drive, Ames, IA 50011-3212, USA. E-mail: beresnev@iastate.edu

integrand in Eq. (1) is reduced to an analytical form (Aki & Richards, 1980, their Eq. 14.37), recast and analyzed in the form convenient for numerical integration by Beresnev (2017b, his Eq. 1). For brevity, we refer the reader to the original publications for the exact shape of the integral.

In the following, the representation integral in this form will be used to conduct the sensitivity analyses and the resulting uncertainties associated with the typical size of the grid used in the inversions and the adoption of static slip as the only governing parameter of the slip (source time) function (STF). Specification of the moment tensor m_{pq} requires adopting a model of STF. To begin with, we will formulate the two forms of STFs that are typical in earthquake ground-motion studies.

2. The Source Time Functions

2.1. Triangular Slip-Velocity Function

In most published inversions, the slip-velocity function (SVF) (first derivative of the STF) is chosen in the form of an isosceles triangle of height v_m and base (duration) t_0, where v_m is the maximum velocity (peak rate) of slip. If $\Delta u(t)$ is the temporal shape of fault displacement, and U is the final slip, the triangular SVF has the form

$$\Delta\dot{u}(t) = 2v_m \frac{t}{t_0}, 0 \le t < \frac{t_0}{2} \tag{2a}$$

$$\Delta\dot{u}(t) = 2v_m \left(1 - \frac{t}{t_0}\right), \frac{t_0}{2} \le t < t_0 \tag{2b}$$

where

$$t_0 = \frac{2U}{v_m}. \tag{3}$$

Equations (2a) and (2b) are plotted in convenient non-dimensional form in Fig. 1.

In the far field, ground displacement is controlled by the fault-slip velocity. The temporal shape of the far-field ground-velocity pulse, therefore, is the second derivative of the STF:

$$\Delta\ddot{u}(t) = \frac{v_m^2}{U}, 0 \le t < \frac{t_0}{2} \tag{4a}$$

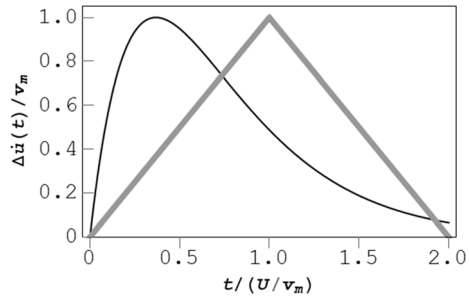

Figure 1
The triangular and ω^2 slip-velocity functions

$$\Delta\ddot{u}(t) = -\frac{v_m^2}{U} \cdot \frac{t_0}{2} \le t < t_0 \tag{4b}$$

It has a highly idealized rectangular form.

As Eq. (3) demonstrates, for given magnitude and the respective average displacement, assuming a certain value of the duration t_0 of the triangle, as typically done in performing the inversions (Beresnev, 2003), is equivalent to fixing v_m.

2.2. ω^2 Function

A more realistic source time function, popular in strong ground-motion simulations, is the one that produces the ω^2 seismic spectrum in the far field (Beresnev & Atkinson, 1997, their Eq. 6; Beresnev, 2001, his Eqs. 1 and 3; Aagaard & Heaton, 2004, their Eq. 1; Gallovič & Brokešová, 2004, their Eq. 14; Aagaard et al., 2008, their Eqs. 1–2). Its asymmetric far-field ground-velocity pulse is

$$\Delta\ddot{u}(t) = e^2 \frac{v_m^2}{U} e^{-t/\tau} \left(1 - \frac{t}{\tau}\right), \tag{5}$$

where

$$\tau = \frac{U}{e v_m} \tag{6}$$

[we keep referring to the second derivative of $\Delta u(t)$ as "ground velocity", even though it has the units of acceleration, because the shape of the pulse in the far field is proportional to $\Delta\ddot{u}(t)$]. The respective ω^2 SVF $\Delta\dot{u}(t)$ is also plotted in Fig. 1; it is the same as given by Beresnev (2022a), his Eq. 9

and Fig. 1). Comparison of Eqs. (3) and (6) shows that t_0 and τ play the role of the equivalent duration parameters (the slip rise times).

Beresnev (2022a) showed that the ω^2 pulse is equivalent to the source time functions derived from numerical rupture-dynamics simulations.

2.3. Dependence of Source Time Functions on Two Parameters

An important similarity between the triangular (Eqs. 4a, 4b) and the ω^2 (Eq. 5) ground-velocity pulses in the context of the present analysis is that both are fundamentally controlled by two physical parameters of faulting: the static slip U and the peak slip velocity v_m. For the ω^2 pulse, the reduction to the functional dependence on just U is only achieved at the low-frequency range, $\omega \ll \omega_c$, where ω_c is the corner frequency of the Fourier spectrum, $\omega_c = 1/\tau$.

The amplitude Fourier spectrum of the triangular pulse (Eqs. 2a, 2b) is the squared sinc function (Beresnev, 2003, his Eq. 7): $\Delta\dot{u}(\omega) = U\left[\frac{\sin(\omega t_0/4)}{\omega t_0/4}\right]^2$. The values of the squared expression in the brackets are close to unity at the very low frequencies only. The sinc function in the brackets has its first null at the frequency $f_N = 2/t_0 = v_m/U$, toward which it precipitously diminishes from one to zero. The quantity f_N, therefore, can be considered an equivalent of the corner frequency f_c, introduced for the ω^2 source, now for the triangular source. At all frequencies approaching or greater than f_c or f_N, respectively, a dependence of STFs on two parameters is inevitable; as Eqs. 4a, 4b and 5 demonstrate, the squared dependence on v_m is much stronger than the linear one on U in both cases. These equations also show that v_m and U clearly trade off with each other.

For the triangular function typically used in the inversions, therefore, to avoid ambiguity and ensure that the inverted data are only controlled by the slip, the frequency range of the data should be reduced to the values much lower than f_N. The difficulty associated with such an approach is that f_N itself depends on the maximum slip velocity and is thus unknown.

3. Sensitivity of Fault Radiation to the Size of Discretization Grid

3.1. Procedure

Having the forms of the source time functions defined, we can proceed to the sensitivity analyses formulated as the goals of the paper. We will first address the uncertainty that may result from the assumed discretized-cell size on the fault.

As pointed out by Beresnev (2003), there have been no clearly established criteria for setting the subfault size used to discretize the representation integral (Eq. 1) in the various inversion studies. Most inversions have tended to follow an ad-hoc approach, in which the cell size scaled with the magnitude of the earthquake for the technical reasons of keeping the inversion problem stable and computationally tractable. For example, subfault dimensions of 3×2.5 km^2 were used for a $M \approx 7$ event (Hartzell & Heaton, 1983), while the dimensions increased to 25×25 km^2 for $M \approx 9$ (Yoshida et al., 2011) (more examples are given by Beresnev, 2003). The possibility of inadequate fault discretization adversely affecting source-inversion results was pointed out by Hisada (2001, the author's Figs. 7 and 8). We can evaluate the basis for the specific cell-size choices by investigating the convergence of the integral sum in the discretized integral in Eq. (1).

Our analyses are conducted for a M_w 7 earthquake on a right-lateral strike-slip fault with the length $L = 50$ km and width $W = 15$ km along strike and dip, respectively, according to the empirical relationship between the rupture area and moment magnitude of Wells and Coppersmith (1994, their table 2A). The average offset $U = 2.1$ m was calculated as $U = M_0/(\mu A)$, where the moment M_0 was obtained from the moment magnitude and the fault area A from the equation of Wells and Coppersmith. The shear modulus μ was calculated as $\mu = \beta^2\rho$, where the density ρ was taken as 2700 kg/m^3 and the shear-wave velocity β obtained from the P-wave velocity of 5000 m/s as $\beta = 5000/\sqrt{3}$ m/s.

Similarly to Beresnev (2017a, his Fig. 2), the complexity in the distribution of static slip was introduced by superimposing a sinusoidal modulation and a random component on the constant U:

$U(\xi_1, \xi_2) = U[1 + 0.5\sin k_L\ \xi_1 \sin k_W \xi_3 + 0.5\eta(\xi_1, \xi_3)]$, where ξ_1 and ξ_3 are along the strike and dip, respectively. The random variable $\eta(\xi_1, \xi_3)$ was drawn from a normal distribution with zero mean and standard deviation of 0.06, constrained to equal –1 if its value accidentally fell below –1. The sinusoidal disturbance had the wavelengths $\lambda_L = L/60$ and $\lambda_W = W/16$ (0.83 and 0.94 km, respectively). Its amplitude was $0.5U$. The wavenumbers are $k_L = 2\pi/\lambda_L$ and $k_W = 2\pi/\lambda_W$. The quantity $U(\xi_1, \xi_2)$ was realistically generated on a grid with a step of $\lambda_L/20$ and $\lambda_W/20$ in each respective direction ξ_1 and ξ_3 and then interpolated by a third-order polynomial during the numerical evaluation of the integral. The rupture proceeded radially with the constant speed of 0.8β from the hypocenter in the center of the fault (with the coordinates $L/2$ and $-W/2$, the origin and orientation of the axes being as in Beresnev, 2017b, his Fig. 1).

The omega-square STF $\Delta u(t)$, corresponding to $\Delta\ddot{u}(t)$ in Eq. (5), was used (Beresnev & Atkinson, 1997, their Eq. 6), with the variable function $U(\xi_1, \xi_2)$ in Eq. (5). The rise time τ (inverse of corner frequency) was calculated from Eq. (6) with $U(\xi_1, \xi_2)$ in it, in which v_m was set to a typical constant value of 1 m/s (Beresnev, 2022b). In the slip model thus generated, both the final slip and the rise time (corner frequency) were heterogenized in both the deterministic and stochastic manner. The average corner frequency, calculated from Eq. (6) as $f_c = (e \times 1/2.1)/(2\pi)$, is 0.21 Hz.

The fault-normal component of the radiated displacement, which typically is the larger component of ground motion, was computed by the numerical integration in Eq. (1) with the sampling interval of 0.02 s. The integration procedure is described by Beresnev (2017b), except that a fixed subfault size was used, as in the slip-inversion studies, instead of an adaptive mesh. Accordingly, the fault was discretized into rectangular cells, and the integral was computed for each term in the integrand as the sum $\sum(I\Delta\Sigma)$ over all subfaults, where I is the value of the respective term in the integrand at the subfault center and $\Delta\Sigma$ is the subfault area (the same symbol Σ is used for the summation sign and the area). The reversal of the order of integration and differentiation in the far-field terms of the integrand was applied as described by Beresnev (2017b).

A view exists that discretizing the fault into subelements for the purpose of the numerical evaluation of integral (1) indicates that the subfaults are assumed to be point sources and should then be smaller than the radiated wavelengths (Chen et al., 2019, pp. 371–372). This is not the case. Green's tensor in (1), by definition, is always calculated for a point source (the delta function) and hence cannot restrict the subfault size in the sense that no element can be a spatial delta function. No assumption about the individual cells being points is made in evaluating the continuous integral by its integral sum. The only factor limiting the grid dimension is the numerical convergence of the summation, bearing no restriction on the radiated wavelength. As long as the integral sum converges within a given numerical precision, the field calculated through Eq. (1) is exact, within that precision.

The observation point was placed in the near field at 200 m above the upper corner of the fault and offset by 200 m in the direction perpendicular to the fault plane, as shown in Fig. 1 of Beresnev (2017a). The trace of ground velocity was obtained by numerically differentiating the synthetic displacement seismogram.

4. Results

To compare the effect of the coarseness of the mesh on the results of the numerical integration, we used three grid sizes (the first and the second are the numbers of subfaults along strike and dip, respectively): 17×6, 34×12, and 68×24. The respective subfault dimensions are 2.9×2.5, 1.5×1.25, and 0.74×0.63 km^2. Figure 2 presents the respective synthetic ground-velocity time histories at the observation point. We show the ground velocities, because these are the records that are frequently used in the strong-ground-motion inversions for earthquake-slip distributions (e. g., Hartzell & Heaton, 1983; Hartzell et al., 2007, p. 1916; Yoshida et al., 2011). To further match the procedures adopted in the typical inversion studies, the time histories shown have been high-cut filtered

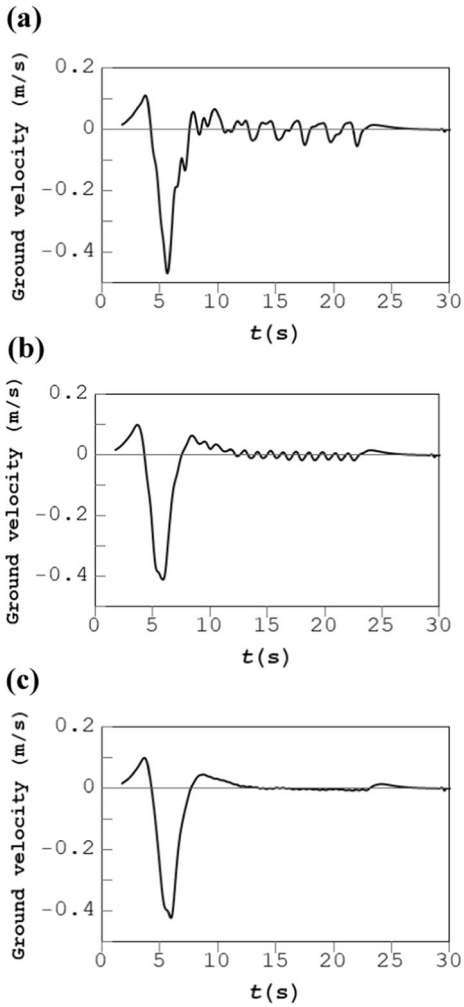

Figure 2
Ground-velocity time histories for the **a** 2.9 × 2.5 km, **b** 1.5 × 1.25 km, and **c** 0.74 × 0.63 km subfaults

above 2 Hz. Figure 2 demonstrates that, for the reasonably heterogeneous slip model considered, the convergence of the integral sum is visually achieved only toward the size of 0.74 km × 0.63 km (Fig. 2c), comparable to the size of the deterministic (sinusoidal) disturbance, while the coarser dimensions of 2.9 × 2.5 km (Fig. 2a) lead to significant unphysical oscillations caused by the numerical error. Any greater sizes would clearly be grossly inadequate.

If the time history in Fig. 2c is the true ground motion, the 17 × 6 fault discretization (Fig. 2a) is unable to correctly reproduce it. Any realistic inversion using this size will nonetheless attempt to find a slip model matching the true seismogram, resulting in an incorrect slip image. The differences occur mostly in the tail of the pulse; to match them, small-scale fault heterogeneity may be required to fit these artificial oscillations. Such heterogeneity will be purely fictitious. The generation of artificial randomly distributed fault roughness, introduced by increasing the subfault size in the inversion, was demonstrated by Hartzell et al., (2007, p. 1919 and their Fig. 4, a1 and b1) by comparing the slip images obtained with the 1 × 1 km and 2 × 2 km subfaults. Hartzell et al. (2007) did not reveal the mechanism behind creating unrealistic complexity, while we emphasize here that it is in the choice of the grid that does not lead to the convergence of the integral. In reality, because the true slip distribution is always unknown, the adequate grid size cannot be even established with certainty.

Furthermore, even if the size of the grid leads to a precise solution of the forward problem, this does not guarantee the correctness of the generally ill-posed and non-unique inversion. Generally, therefore, the use of every particular inversion algorithm must be accompanied by careful tests with the generation of synthetic fields from known sufficiently complex fault-slip models to make sure that the inversion indeed resolves the correct distribution.

In addition to Fig. 2, we also ran scenarios in which (1) the slip distribution $U(\xi_1, \xi_2)$ was sampled at smaller steps of $\lambda_L/60$ and $\lambda_W/60$ or (2) the standard deviation in the random variable $\eta(\xi_1, \xi_3)$ was doubled to 0.12. No visual differences with the results presented in Fig. 2 were found.

All subsequent illustrations will use the same original slip model and will be produced with the 68 × 24 mesh.

5. *Trade-Offs Between Static Slip and Slip Velocity*

Our second goal is to analyze the uncertainties in the resolved slip caused by the dependence of radiation on two parameters, both U and v_m, rather than U only. The resulting ambiguity can be characterized in two ways. First, trade-offs are possible, whereby different values of static slip may produce similar radiation if their effect is offset by the respective variations in slip velocity. Second, if slip is the only governing parameter, then keeping it constant and

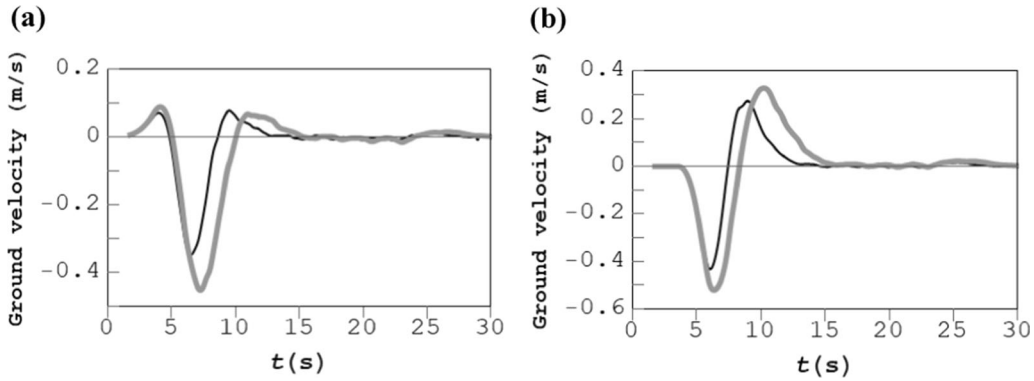

Figure 3
a Ground-velocity pulses, obtained from the triangular slip-velocity function, in case of $U = 2.1$ m, $v_m = 1$ m/s (black curve) and $U = 2 \times 2.1$ m, $v_m = \sqrt{2} \times 1$ m/s (gray curve). **b** Same as (**a**) but for only the far-field terms retained in the integration

varying the slip velocity should not affect the radiation. We will carry out the tests of both kinds, using both the triangular and omega-square slip functions. For the triangular SVF, the heterogenized rise time t_0 will be calculated from Eq. (3), in which the same variable function $U(\xi_1, \xi_2)$ is used as in Eq. (6) before. All seismograms are again high-cut filtered above 2 Hz.

5.1. *Triangular Slip-Velocity Function*

5.1.1 *Trade-Off Between Slip and Slip Velocity*

One observes from Eqs. (4a, 4b) that the far-field ground-velocity pulse, corresponding to the triangular SVF, is controlled by the ratio v_m^2/U. To illustrate the trade-off, we will keep the ratio constant by simultaneously changing the earlier values of U and v_m, used to produce the example of Fig. 2, by multiplying v_m by $\sqrt{2}$ and U by 2. Figure 3a shows the two synthetic pulses, computed from the representation integral, one with the original and one with the modified parameters as explained (black and gray lines, respectively). For the original and the modified pulses, the average frequencies of the first null in the spectrum are $f_N = 0.48$ Hz and 0.34 Hz, respectively. The comparison shows that, despite an increase in the average static slip by a factor of two for the gray curve, the curve is only slightly different from the original one. In case of real seismic data, contaminated by both coherent and incoherent noise, the difference may be unnoticeable, causing one to believe that the slip weights that produced the pulses were nearly the same.

Figure 3a was generated using the full expression of the representation integral, containing both the near- and far-field terms in the integrand. The standard methods of inversion only retain the far-field portion, in which only the terms with $\Delta\dot{u}(t)$ appear in the integrand (Hartzell & Helmberger, 1982, their equation on p. 578; Heaton, 1982, his equation A2). Accordingly, the same example was recalculated with only the part of the integrand containing $\Delta\dot{u}(t)$ (the fourth and fifth terms in the integrand of Aki & Richards, 1980, their Eq. 14.37) (Fig. 3b). The curves can be argued to be even closer in their amplitudes, despite the difference in the average slip of a factor of two.

5.1.2 *Dependence of Radiation on Slip Velocity*

In Fig. 4, the original value of U is retained, but the slip velocity is doubled. As in Fig. 3, the comparison is between the original (black curve) and the modified (gray curve) values of the parameters, separately for the full integral (Fig. 4a) and its far-field terms only (Fig. 4b). The comparison reveals a significant dependence of the pulse on slip velocity, U being equal, as one would expect from the quadratic dependence on v_m in Eq. (4). An inversion of such data solely for U would result in a significantly overpredicted resolved slip in case of the gray line,

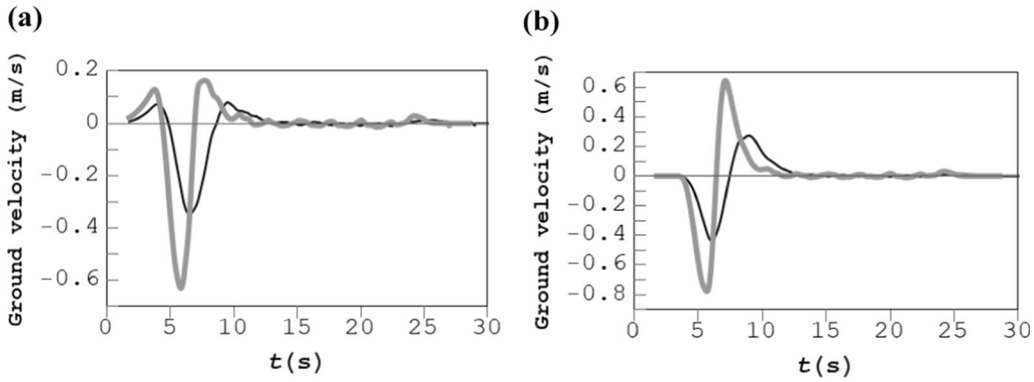

Figure 4
a Ground-velocity pulses, obtained from the triangular slip-velocity function, in case of U = 2.1 m, v_m = 1 m/s (black curve) and U = 2.1 m, v_m = 2 × 1 m/s (gray curve). **b** Same as (**a**) but for only the far-field terms retained in the integration

whereas in reality the slip is the same in both cases. Inclusion of only the far-field terms in the integration exacerbates the difference in the amplitudes (Fig. 4b).

5.2. *Omega-Square Slip-Velocity Function*

Figures 5 and 6 are the equivalents of Figs. 3 and 4, respectively, now calculated for the ω^2 slip function, with the same corresponding values of the parameters U and v_m. The black lines in Figs. 5a and 6a hence are the same as that in Fig. 2c. The general conclusions regarding the trade-offs between the slip and slip velocity and the resulting ambiguity in the inversions, drawn from Figs. 5 and 6, remain the same, although the trade-offs in this case are somewhat less severe than in the case of the triangular SVF. Note that the triangular slip function is the one used in ground-motion inversions.

6. *Conclusions*

Our goals have been to analyze the sensitivity of fault radiation to (1) the selection of the cell size used to discretize the fault plane and (2) the choice of a particular duration of subfault slip. A heterogeneous fault model has been used, containing both the deterministic and stochastic components.

The subfault dimensions of approximately 3 × 2.5 km, significantly greater than the characteristic size of the deterministic fault-slip disturbance, result in unphysical oscillations in radiation caused by the integration error, which gradually diminish with the reduction in cell size. Any greater subfaults would not adequately represent the true radiation; matching the seismic field with the mesh that is too coarse will lead to distorted slip images.

Two rupture parameters control earthquake radiation, except at the very low frequencies: the static offset U and the maximum slip rate v_m. The dependence on v_m is much stronger than on U. The standard methods invert solely for earthquake slip, assuming a certain slip duration equivalent to fixing v_m. The two parameters trade off with each other, resulting in a significant uncertainty in the resolved slip images depending on what particular value of slip velocity had been implicitly adopted. Practically indistinguishable ground-velocity pulses can be produced by the average slips that are different by a factor of two, if the offsetting slip-rate value is simultaneously modified only by a factor of $\sqrt{2}$. Alternatively, the same value of average slip on the fault can produce conspicuously different amplitude differences in the radiated ground-velocity pulses, depending on the underlying choice of slip rate. An inversion of such data would misinterpret such differences as a result of much greater slip.

The artifacts potentially produced are generally exacerbated by the use of the triangular slip-velocity function, if compared to the ω^2 SVF, as well as the

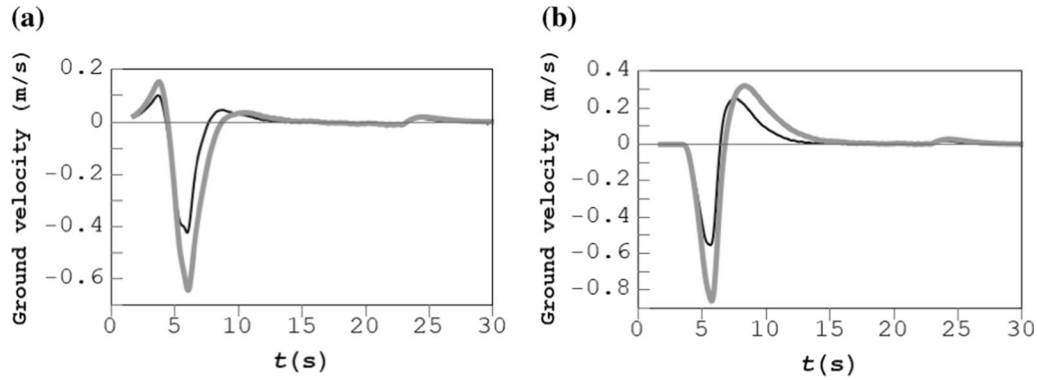

Figure 5
a Ground-velocity pulses, obtained from the omega-square slip-velocity function, in case of $U = 2.1$ m, $v_m = 1$ m/s (black curve) and $U = 2 \times 2.1$ m, $v_m = \sqrt{2} \times 1$ m/s (gray curve). **b** Same as (**a**) but for only the far-field terms retained in the integration

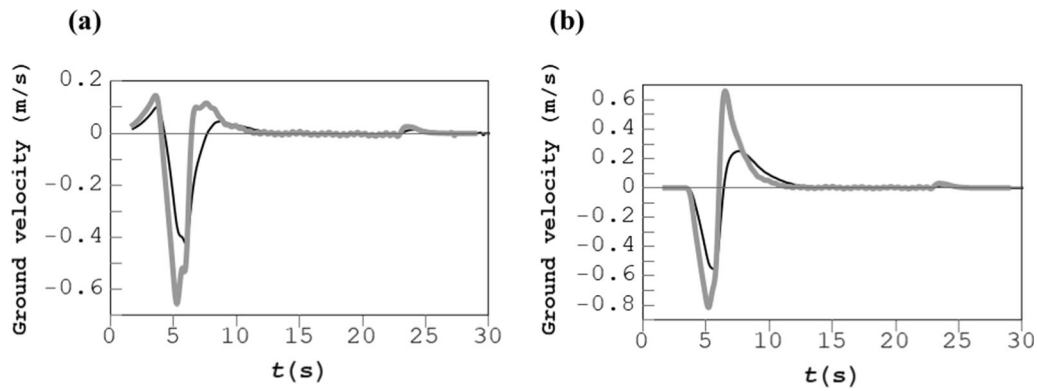

Figure 6
a Ground-velocity pulses, obtained from the omega-square slip-velocity function, in case of $U = 2.1$ m, $v_m = 1$ m/s (black curve) and $U = 2.1$ m, $v_m = 2 \times 1$ m/s (gray curve). **b** Same as (**a**) but for only the far-field terms retained in the integration

retention of only the far-field terms in the inversion's matrix equation.

The only way to avoid ambiguity in the inverted images, caused by the simultaneous dependence on two rupture parameters, is to limit the analyses to very low frequencies, much lower than f_N for the case of the triangular function. The values of f_N for the examples in Fig. 3 are 0.48 and 0.34 Hz. The analyzed data would hence need to be low-pass filtered to frequencies much lower than 0.5 Hz, approximately. For relatively moderate magnitudes, such severe frequency restriction may be sufficient to reduce the fault to a point source, precluding the possibility to reveal the finite fault structure. As an illustration, in case of a unidirectional small (Haskell) rupture, the effects of fault finiteness are in the multiplication of the point-source spectrum by a sinc function (Aki & Richards, 1980, their Eq. 14.18). A straightforward calculation shows that, for the fault dimensions corresponding to a M_w 7 earthquake and the shear-wave radiation forward, the sinc function is significantly different from unity at the frequencies greater than approximately 0.2 Hz, meaning that those frequencies are needed to resolve the fault finiteness. Such a requirement conflicts with the need to restrict frequencies to much lower than 0.5 Hz to

make the inversion independent of the assumptions regarding the slip rate. Further compounding the difficulty is the fact that the values of f_N given are based on v_m = 1 m/s. Observations indicate that peak slip velocities on the order of 0.1 s are also possible (Beresnev, 2022b), which will reduce f_N to 0.048 Hz and 0.034 Hz. Such a low-frequency band of the data would reduce the model of even a M_w 7 earthquake to a point source.

Hartzell et al., (2007, p. 1919 and their Fig. 4, a1 and a2) verified the independence of their inversion results, using the triangular slip-velocity function, on the alternative durations t_0 of 0.2 and 0.4 s, with their data low-passed at 2 and 1 Hz, respectively. The values of f_N in these cases are 10 and 5 Hz, respectively; the frequency range of their analyses was hence much lower than f_N, as required. They examined the M_w 6 2004 Parkfield earthquake. From the Wells-Coppersmith relation, an average fault offset in this case is U = 0.49 m. However, using v_m = 0.1 m/s, one would obtain t_0 = 9.8 s (Eq. 3) and f_N = 0.20 Hz. Such a low value of f_N is equally plausible, which would force the authors to restrict their band to much lower than 0.2 Hz. However, for a M_w 6 earthquake at such frequencies, the sinc function carrying the effects of fault finiteness is very nearly equal to one, precluding any analysis of finite fault structure.

We stress that the choice of the triangle duration t_0 in the inversions cannot be arbitrary but is inherently tied to the reasonable expectations about the slip U and slip velocity v_m.

In this article, we have only addressed the most prevalent inversion algorithms based on the solution of linear matrix equations, in which the slip weights are the only unknowns. The methods of minima search in the parameter space, allowing solutions for multiple source parameters, known as "nonlinear" inversion algorithms, are being developed but have not undergone similar widespread usage (Beresnev, 2003, p. 2457).

Acknowledgements

The author is indebted to two anonymous reviewers for the comments on the manuscript.

Author contributions IAB has contributed to this work.

Funding

No funding was provided for the completion of this study.

Data availability

No data were used in the paper. All inferences were made through the analyses of the respective equations and literature sources as indicated.

Declarations

Conflict of interest The authors declare no competing interests.

References

Aagaard, B. T., Brocher, T. M., Dolenc, D., Dreger, D., Graves, R. W., Harmsen, S., Hartzell, S., Larsen, S., & Zoback, M. L. (2008). Ground-motion modeling of the 1906 San Francisco earthquake, part I: validation using the 1989 Loma Prieta earthquake. *Bulletin of the Seismological Society of America, 98*, 989–1011.

Aagaard, B. T., & Heaton, T. H. (2004). Near-source ground motions from simulations of sustained intersonic and supersonic fault ruptures. *Bulletin of the Seismological Society of America, 94*, 2064–2078.

Aki, K., & Richards, P. G. (1980). *Quantitative seismology*. San Francisco: W. H Freeman and Company.

Beresnev, I. (2013). Reflections on frequency dependence in earthquake-source inversions. *Natural Hazards, 66*, 1287–1291.

Beresnev, I. A. (2001). What we can and cannot learn about earthquake sources from the spectra of seismic waves. *Bulletin of the Seismological Society of America, 91*, 397–400.

Beresnev, I. A. (2003). Uncertainties in finite-fault slip inversions: To what extent to believe? (A critical review). *Bulletin of the Seismological Society of America, 93*, 2445–2458.

Beresnev, I. A. (2017a). Factors controlling high-frequency radiation from extended ruptures. *Journal of Seismology, 21*, 1277–1284.

Beresnev, I. A. (2017b). Simulation of near-fault high-frequency ground motions from the representation theorem. *Pure and Applied Geophysics, 174*, 4021–4034.

Beresnev, I. A. (2022a). Equivalence between ω^n source time functions and those proposed from dynamic finite-source modeling. *Bulletin of the Seismological Society of America, 112*, 1886–1893.

Beresnev, I. A. (2022b). The strongest possible earthquake ground motion. *Journal of Earthquake Engineering, 26*, 563–572.

Beresnev, I. A., & Atkinson, G. M. (1997). Modeling finite-fault radiation from the ω^n spectrum. *Bulletin of the Seismological Society of America, 93*, 67–84.

Chen, Y.-T., Zhang, Y., & Xu, L.-S. (2019). Inversion of earthquake rupture process: theory and applications. *Rivista Del Nuovo Cimento, 42*, 367–406.

Gallovič, F., & Brokešová, J. (2004). On strong ground motion synthesis with k^{-2} slip distributions. *Journal of Seismology, 8*, 211–224.

Hartzell, S., & Helmberger, D. V. (1982). Strong-motion modeling of the imperial valley earthquake of 1979. *Bulletin of the Seismological Society of America, 72*, 571–596.

Hartzell, S., Liu, P., Mendoza, C., Ji, C., & Larson, K. M. (2007). Stability and uncertainty of finite-fault slip inversions: application to the 2004 Parkfield, California, earthquake. *Bulletin of the Seismological Society of America, 97*, 1911–1934.

Hartzell, S. H., & Heaton, T. H. (1983). Inversion of strong ground motion and teleseismic waveform data for the fault rupture history of the 1979 Imperial Valley, California, earthquake. *Bulletin of the Seismological Society of America, 73*, 1553–1583.

Heaton, T. H. (1982). The 1971 San Fernando earthquake: a double event? *Bulletin of the Seismological Society of America, 72*, 2037–2062.

Hisada, Y. (2001). A theoretical omega-square model considering spatial variation in slip and rupture velocity. Part 2: case for a two-dimensional source model. *Bulletin of the Seismological Society of America, 91*, 651–666.

Wells, D. L., & Coppersmith, K. J. (1994). New empirical relationships among magnitude, rupture length, rupture width, rupture area, and surface displacement. *Bulletin of the Seismological Society of America, 84*, 974–1002.

Yoshida, Y., Ueno, H., Muto, D., & Aoki, S. (2011). Source process of the 2011 off the Pacific coast of Tohoku Earthquake with the combination of teleseismic and strong motion data. *Earth, Planets and Space, 63*, 565–569.

(Received November 7, 2022, revised December 6, 2022, accepted December 12, 2022, Published online December 23, 2022)